The Planetary Science Journal, 2:136 (15pp), 2021 August https://doi.org/10.3847/PSJ/abfec6

The Scientific Value of a Sustained Exploration Program at the Aristarchus Plateau

Timothy D. Glotch[1], Erica R. Jawin[2], Benjamin T. Greenhagen[3], Joshua T. Cahill[3], David J. Lawrence[3], Ryan N. Watkins[4,5], Daniel P. Moriarty[6], Nandita Kumari[1], Shuai Li[7], Paul G. Lucey[7], Matthew A. Siegler[8,9], Jianqing Feng[8], Laura B. Breitenfeld[1], Carlton C. Allen[10,12], Hanna Nekvasil[1], and David A. Paige[11]

[1] Department of Geosciences, Stony Brook University, Stony Brook, NY 11794-2100, USA; timothy.glotch@stonybrook.edu
[2] Smithsonian Institution, National Museum of Natural History, Washington, DC 20560, USA
[3] Applied Physics Laboratory, Johns Hopkins University, Space Exploration Sector, Laurel, MD 20723, USA
[4] Arctic Slope Regional Corporation Federal, Beltsville, MD 20705, USA
[5] NASA Headquarters, Washington, DC 20546, USA
[6] NASA Goddard Space Flight Center, Mail Code 698, Greenbelt, MD 20771, USA
[7] Hawaii Institute of Geophysics and Planetology, University of Hawaii, Honolulu, HI 96822, USA
[8] Planetary Science Institute, Tucson, AZ 85719, USA
[9] Roy M. Huffington Department of Earth Sciences, Southern Methodist University, Dallas, TX 75275-0395, USA
[10] NASA Johnson Space Center, Astromaterials Research and Exploration Science Division, Houston, TX 77058, USA
[11] Department of Earth, Planetary, and Space Sciences, University of California at Los Angeles, Los Angeles, CA 90095-1567, USA
Received 2020 November 26; revised 2021 May 5; accepted 2021 May 5; published 2021 July 26

Abstract

The Aristarchus plateau hosts a diversity of volcanic features, including the largest pyroclastic deposit on the Moon, the largest sinuous rille on the Moon, and intrusive and extrusive examples of evolved, Th-rich silicic lithologies. We provide an overview of previous remote-sensing measurements of the Aristarchus plateau and provide new analyses of Diviner Lunar Radiometer thermal IR data, Lunar Prospector Gamma Ray Spectrometer Th data, Chang'e-5 Microwave Radiometer data, and hyperspectral and multispectral visible/near-infrared images and spectra from the Chandrayaan-1 Moon Mineralogy Mapper and the Kaguya Multispectral Imager. The rich diversity of volcanic features on the Aristarchus plateau presents an opportunity for a sustained science and exploration program. We suggest a series of missions to the Aristarchus crater floor or ejecta, the Cobra Head, and Herodotus Mons to investigate the link between pyroclastic, effusive basaltic, and silicic volcanism in the region. Such missions would enable analyses of silicic rocks that are rare in the Apollo sample collection and demonstrate in situ resource utilization of FeO- and H_2O-bearing pyroclastic materials.

Unified Astronomy Thesaurus concepts: The Moon (1692); Lunar science (972); Lunar evolution (952); Volcanoes (1780)

1. Introduction

The Aristarchus plateau, located on the lunar nearside in central Oceanus Procellarum, rises up to 3 km above the surrounding mare surface. It is likely a block of ancient highlands crust that was uplifted during the Imbrium basin-forming impact (Wilhelms 1987). Alternatively, Spudis et al. (2013) interpreted it as a large, partially developed shield volcano complex that did not fully bury the highlands block on which it was constructed. The plateau hosts one of the highest concentrations of diverse volcanic features on the Moon. This includes pyroclastic deposits formed from explosive volcanic eruptions (Zisk et al. 1977); sinuous rilles carved by turbulent, erosive lava flows (Hurwitz et al. 2013); unusual volcanic features termed "irregular mare patches" (IMPs) that may represent the youngest lunar volcanic deposits (Braden et al. 2014); and numerous domes and exposures that in some cases formed from compositionally evolved, silicic melt compositions (Glotch et al. 2010). The diverse volcanic features resulted from multiphased volcanism in the region, likely making it unique on the Moon. These features represent end-members on the spectrum of traditional volcanic eruption styles (e.g., explosive and effusive), ages (Nectarian to Copernican), and compositions (mafic to silicic); however, they all provide a critical window into the characteristics, diversity, and evolution of the lunar interior through space and time. The large number of volcanic features may be tied to elevated concentrations of heat-producing elements in the region (Hagerty et al. 2009). Critically, the Aristarchus plateau hosts or is immediately adjacent to each of these types of end-member volcanism, including the Moon's widest and deepest sinuous rille, Vallis Schröteri (Hurwitz et al. 2013); the largest pyroclastic deposit, which is rich in iron- and water-bearing volcanic glass (Gaddis et al. 2003; Milliken & Li 2017); exposed silicic material that may indicate the presence of an excavated granitic or rhyolitic volcanic complex (Glotch et al. 2010; Mustard et al. 2011); very young mare basalts (Hiesinger et al. 2011); and at least one IMP (Braden et al. 2014).

A sustained exploration strategy focused on lunar volcanism at the Aristarchus plateau would address many high-priority lunar science goals as defined by the lunar science and exploration community (Jawin et al. 2019) and improve our understanding of volcanism throughout lunar geologic history. The plateau's location on the lunar nearside, as well as its large size, shallow slopes, and high bearing capacity (Bickel et al. 2019), enable easy access for future robotic and/or human exploration. The expansive pyroclastic deposit is well suited for closing strategic knowledge gaps regarding operating on the

[12] Retired.

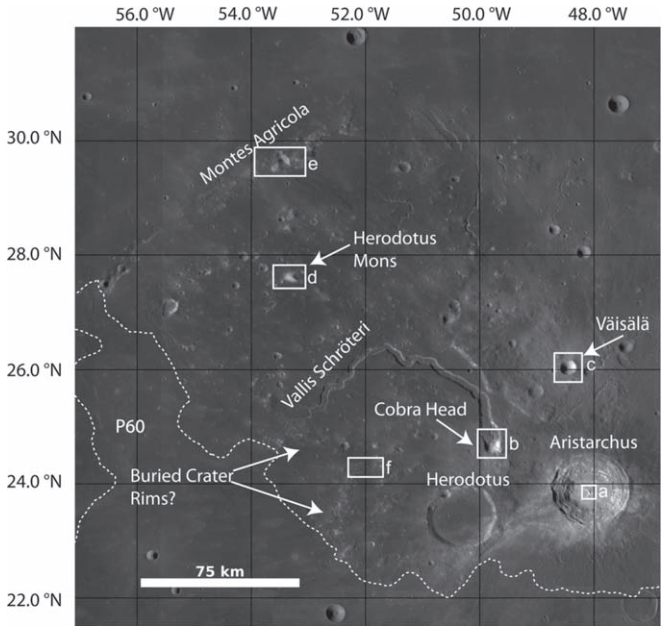

Figure 1. The LROC WAC mosaic of the Aristarchus plateau and major features. Boxes indicate positions, and letter labels correspond to the image order of LROC NAC mosaics in Figure 10. The dotted line approximates the boundary of the P60 young mare basalt unit (Hiesinger et al. 2011).

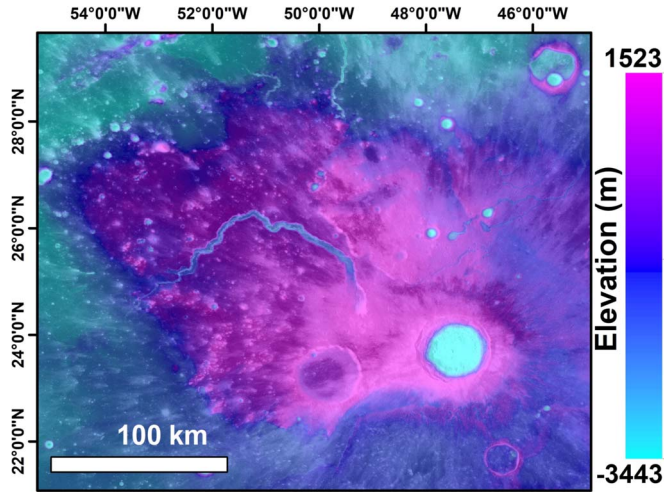

Figure 2. Blended LOLA/SELENE TC topography of the Aristarchus region overlaid on a WAC mosaic.

lunar surface and is also enriched in useful resources, including water and iron, enabling in situ resource utilization (ISRU). High-temperature hydrogen reduction experiments have shown that the FeO-rich pyroclastic glasses release the highest percentage of oxygen of any Apollo soils (Allen et al. 1996), making these deposits promising lunar resources. The combination of scientific interest and resource potential has kept pyroclastic deposits among the best-studied prospects for a future lunar base (Coombs et al. 1998). The Aristarchus plateau is therefore the ideal location on the Moon to explore the diversity of lunar volcanism in one accessible, traversable region.

Here we provide a review of previous remote-sensing investigations of the Aristarchus plateau, present new remote-sensing measurements, and describe the physical, mineralogical, and chemical characteristics of important features on the Aristarchus plateau. The rich diversity of geologic structures on the plateau necessitates a sustained exploration program to untangle the complicated geologic history and determine the resource potential of the region. We suggest a hyperspectral thermal infrared (TIR) imager and gamma-ray and neutron spectrometer (GRNS) payload for an initial future Commercial Lunar Payload Services (CLPS) mission to Aristarchus, perhaps supplemented by a visible/near-infrared (VNIR) hyperspectral imager or multispectral camera system. Numerous features on the plateau present compelling science and exploration targets. A landing site close to Herodotus Mons, a silicic dome ~185 km northwest of the center of the Aristarchus crater, would allow a lander or rover to characterize the mineralogy and geochemistry of rare silicic materials, as well as glasses from the largest pyroclastic deposit on the Moon.

2. Major Characteristics of the Aristarchus Plateau

The major features of the Aristarchus plateau are shown in Figure 1. The plateau itself is roughly rectangular with dimensions of ~170 × 220 km (Zisk et al. 1977). The blended LRO Lunar Orbiter Laser Altimeter (LOLA)/SELENE (Kaguya) Terrain Camera (TC) digital elevation model (Barker et al. 2016) shows that the southeast plateau is the highest area of the region and sits ~3500 m above the surrounding mare (Figure 2). The whole plateau slopes downward to the northwest, where the northern margin is ~1000 m above the surrounding mare. The southern portion of the plateau is dominated by the Aristarchus and Herodotus craters. The plateau is bounded on the northwestern margin by the Montes Agricola, a linear ridge roughly radial to the Imbrium basin, with the orthogonal margins concentric to Imbrium, suggesting uplift and emplacement of the plateau related to the Imbrium impact (Zisk et al. 1977).

The northern two-thirds of the plateau is blanketed by a dark mantling deposit that is interpreted to be the largest pyroclastic deposit on the Moon (~50,000 km^2; Gaddis et al. 2003), formed during the early period of mare volcanism (Campbell et al. 2008).

About 170 km northwest of the Aristarchus crater, Herodotus Mons, a bright, ~900 m high, ~6.5 km long knob, emerges from underneath the surrounding pyroclastic blanket. It was originally interpreted as a fragment of highlands Imbrium ejecta (Zisk et al. 1977), but its shape and mineralogic remote-sensing data suggest that it is an extrusive volcanic cone with an evolved composition (Section 4.2). Weitz et al. (1998) estimated that the pyroclastic deposit in many places was mixed with preexisting highland or mare material, and that one of the highest concentrations of pyroclastic glass is located near Herodotus Mons. More recently, Chevrel et al. (2009) calculated that much of the plateau was covered by >90% dark mantling pyroclastic material.

The plateau hosts numerous sinuous rilles, including Vallis Schröteri, the widest and deepest sinuous rille on the Moon. Initiating at a depression referred to as "Cobra Head," the rille is ~4 km wide and ~170 km long, with a nested rille located inside Vallis Schröteri (Hurwitz et al. 2013). The presence of potential spatter cone–like features immediately adjacent to Cobra Head may suggest that the pyroclastic blanket on the plateau erupted from the same source as the lavas that formed the sinuous rille (Head & Wilson 2017), representing a link between explosive and effusive eruptions on the plateau. At the

western terminal margin of Vallis Schröteri, the nested rille cross-cuts the main channel and extends west off the plateau, terminating in Oceanus Procellarum in the potentially very young (~1–2.5 Ga) P60 mare unit (Hiesinger et al. 2011; Stadermann et al. 2018).

3. Background

3.1. Lunar Pyroclastic Volcanism

Over 100 lunar pyroclastic deposits (or "dark mantle deposits," DMDs) have been identified on the Moon that range in size from a few (<10) km^2 to ~50,000 km^2 (the largest being the deposit at Aristarchus; Gaddis et al. 2003; Gustafson et al. 2012). The largest deposits are believed to have formed as a result of long-duration fire fountain ("Hawaiian-style") eruptions (e.g., Head & Wilson 1981) characterized by gas-rich magmas. The co-occurrence of a large pyroclastic deposit and numerous sinuous rilles at Aristarchus suggests very high effusion rates (Head & Wilson 1981, 2017). The volcanic products of these eruptions have suggested to some (e.g., Delano & Livi 1981; Shearer & Papike 1993) that the source regions exceeded >300 km depth and the magma was more primitive (that is, experienced less fractionation) than mare basalts. However, much remains to be learned about the nature of the magmas producing these large pyroclastic deposits. Pyroclastic deposits often contain a large fraction of volcanic glass that was rapidly quenched as it erupted (e.g., Weitz et al. 1998, 1999). These quenched glasses are often rich in iron and titanium, and at least one pyroclastic deposit contains chromium-rich spinel (Sunshine et al. 2010). Returned pyroclastic glass and crystalline beads have also been found to contain coatings of vapor-deposited volatile compounds, including Au, Ag, Cu, Cd, F, S, and Zn (McCubbin et al. 2015), which provide a glimpse of the lunar interior composition and volatile content. Indeed, Head & Wilson (2017) calculated that the magma source for the Aristarchus pyroclastic deposit contained 21,000 ppm of total volatiles. In addition to the volatile-rich coatings on returned samples, remotely sensed data identified evidence of indigenous water within pyroclastic deposits, including Aristarchus, in concentrations of up to several hundred ppm (Milliken & Li 2017).

3.2. Lunar Silicic Volcanism

Remote-sensing observations have identified numerous volcanic structures on the Moon with anomalously silicic, evolved compositions that are likely similar to terrestrial trachytes or rhyolites, although other compositions with SiO_2 contents >~60 wt.% are also possible. These features, originally termed "red spots" and including the Gruithuisen and Mairan domes, among others, were initially identified during the Apollo era and the following decade. They typically have low ultraviolet reflectance with respect to the VNIR portion of the spectrum, low TiO_2 and FeO abundances (Whitaker 1972; Malin 1974; Head & McCord 1978), and high Th abundances (Hagerty et al. 2006). These features also typically have steep edifices (15°–30°), which, along with their spectral characteristics, led researchers to suggest that they formed as a result of nonmare volcanism (Head & Hess 1978; Head & McCord 1978; Chevrel et al. 1999; Hagerty et al. 2006). Chevrel et al. (1999) further suggested that nonmare volcanism may be more expansive in the region, extending beyond the Gruithuisen and Mairan domes.

The silicic compositions of these features were confirmed by the Lunar Reconnaissance Orbiter (LRO) Diviner Lunar Radiometer Experiment, which identified silicic compositional anomalies at the Gruithuisen domes, the Mairan domes, Lassell Massif, Hansteen Alpha, the Compton–Belkovich Volcanic Complex (CBVC), and the Aristarchus crater (Glotch et al. 2010, 2011; Jolliff et al. 2011; Ashley et al. 2016; Boyce et al. 2017). The interpretations of Diviner data are based on analyses of the silicate Christiansen feature (CF) and spectral concavity. The CF is an emissivity maximum, the position of which is indicative of bulk silicate mineralogy (Conel 1969; Logan et al. 1973; Salisbury & Walter 1989). Felsic materials have CF positions at shorter wavelengths, while mafic materials have CF positions at longer wavelengths. Three-point Diviner spectra of silicic materials also display concave-up spectral shapes, which are unique on the Moon and, based on comparison with laboratory mineral and rock spectra, indicate compositions of ⩾~65 wt.% SiO_2 (Glotch et al. 2010, 2017).

The interpretations of these features based on Diviner data are further supported by photometric analyses of Lunar Reconnaissance Orbiter Camera Narrow Angle Camera (LROC NAC) images. In these images, lunar silicic regions exhibit unusually high reflectance and single-scattering albedos, consistent with the presence of quartz and/or alkali feldspar, and minor mafic mineral abundances (Clegg-Watkins et al. 2017).

Silicic samples have been returned by the Apollo astronauts and are generally polymict breccias of multiple compositions, although true granites do exist in the sample collection, characterized by >75 wt.% SiO_2, up to 8 wt.% K_2O, and >60 ppm Th (e.g., Quick et al. 1981; Warren et al. 1983; Seddio et al. 2013, 2014). However, due to limitations in spatial and spectral resolution, it is not clear whether lunar silicic features identified in remote-sensing measurements have the same compositions as these returned samples.

4. Remote-sensing Analyses

4.1. Pyroclastic Deposit

A large portion of the Aristarchus plateau is mantled by a large radar-dark (at 3.8, 12.6, and 70 cm wavelengths) pyroclastic deposit (Zisk et al. 1974, 1977; McEwen et al. 1994; Campbell et al. 2008). This portion of the plateau has the lowest radar reflectivity of anywhere on the Moon (Thompson 1974; Zisk et al. 1974). Like other lunar pyroclastic deposits (e.g., Zisk et al. 1977; Gaddis et al. 1985), the Aristarchus pyroclastic deposits have low same-sense circular (SC) polarization backscatter due to the low abundance of rocks in the deposit that are of similar size to the radar wavelengths.

Although most of the plateau region exhibits low radar backscatter at 70 cm, a region south and east of Vallis Schröteri has higher radar backscatter that was interpreted by Campbell et al. (2008) as a region of thinly mantled basaltic lava flows that spilled over from the Vallis Schröteri rille. The relatively high 12.6 cm radar backscatter over this buried lava flow suggests the presence of numerous rocks 2 cm or larger within the mantling deposit (Campbell et al. 2008). With the exception of this thinly buried lava flow on the plateau, the generally low radar backscatter on the Aristarchus plateau at both 12.6 and 70 cm wavelengths is consistent with a meters-thick, low-density, rock-poor, and TiO_2-poor mantle (Campbell et al. 2008).

The Chang'E 2 Microwave Radiometer (MRM) data set (Siegler et al. 2020) can also be used to constrain the properties of the pyroclastic deposit. MRM collected measurements of the lunar surface with four spectral channels centered at 3.0, 7.8, 19.35, and 37 GHz, equivalent to 10, 3.8, 1.6, and 0.7 cm,

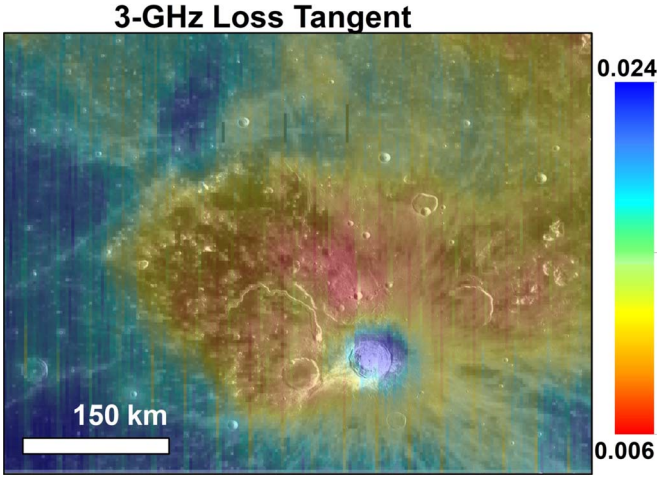

Figure 3. Chang'E 2 MRM 3 GHz loss tangent for the Aristarchus plateau region overlaid on an LROC WAC mosaic.

respectively (Zheng et al. 2012). Recent global-scale analysis of the data set (Siegler et al. 2020) shows the plateau to have low diurnal brightness temperature amplitudes at all observed frequencies, implying a low loss tangent, low-density material (Siegler et al. 2020). For this work, we generated a regional-scale map (~25 km pixel^{-1}) of the Aristarchus plateau region from level 2 calibrated brightness temperature data. The loss tangent values are derived using the model of Siegler et al. (2020) and quantify the transparency of a material to microwave radiation. Figure 3 shows the 3 GHz loss tangent for the Aristarchus region. With the exception of the Aristarchus crater, the whole plateau exhibits loss tangents roughly half that of the surrounding mare, indicating a relatively transparent medium. Combined with loss tangent data at higher frequencies, these data suggest that the plateau is mantled by >5 m of low-TiO_2 material with a lower density than typical highlands.

The color of the Aristarchus pyroclastic deposit was noted by Hevelius (1647) for being red at visible wavelengths compared to the rest of the Moon. Wood (1912) showed that a portion of the plateau has the lowest UV reflectance on the lunar nearside. More recently, Lucey et al. (1986) collected ground-based telescopic data in the 0.6–2.5 μm range for several spots on the plateau and Aristarchus crater. This work suggested that the pyroclastic deposit is composed of >90% Fe^{2+}-bearing glass. Later analyses of Clementine multispectral ultraviolet/visible (UVVIS) data supported these telescopic analyses and showed that the Aristarchus plateau has the reddest color and strongest glass band absorption of any large, regional DMD on the Moon (Weitz et al. 1998). Clementine band ratio plots support the glass-rich interpretation for the Aristarchus pyroclastic deposit and indicate that it falls within the lunar mare compositional range, although its low 415/750 nm reflectance ratio likely indicates a low overall Ti content (consistent with a primitive magma composition) compared to mare basalts and other pyroclastic deposits (Gaddis et al. 2003). Chevrel et al. (2009) used principal components analysis (PCA) to isolate eight spectral units in the Aristarchus region in Clementine UVVIS and NIR data. They found a distinct spectral contribution from the pyroclastic mantle deposit and used an iterative linear mixing model to show that much of the plateau is spectrally homogeneous and up to 90% mantle deposit material. The high modeled abundance of mantle material over much of the plateau is consistent with a thick deposit suggested by the radar and MRM results, as well as the very high effusion rates modeled by Head & Wilson (1981, 2017).

Hyperspectral VNIR imagery from the Chandrayaan-1 Moon Mineralogy Mapper (M^3; Pieters et al. 2009; Green et al. 2011) shows that the extensive pyroclastic deposit in the northern region of the plateau exhibits a shallow 1 μm band depth compared to the pyroxene-dominated mare surrounding the plateau. For most lunar surface materials, the positions of spectral absorption bands near 1 and 2 μm vary systematically with pyroxene composition. In general, short-wavelength absorption bands indicate the presence of Mg-rich, low-Ca pyroxenes (Klima et al. 2007, 2011; Moriarty & Pieters 2016). Absorption bands shift to longer wavelengths with increasing Fe and Ca content. The Aristarchus plateau pyroclastic deposit exhibits different behavior in which the 1 μm band centers exhibit relatively long wavelengths, while the 2 μm band centers exhibit distinctly short-wavelength centers (Figure 4). Together with the relatively shallow absorption band depths, this is characteristic of quenched, Fe-bearing glass, consistent with earlier telescopic and multispectral analyses (e.g., Lucey et al. 1986; Weitz et al. 1998; Gaddis et al. 2003).

Wilcox et al. (2006) employed the Lucey (1998) formulation of the Hapke (1981, 1993, 2001) radiative transfer model to analyze ground-based telescopic data of several large pyroclastic deposits, including the Aristarchus plateau, and determined the compositions, particle sizes, and crystallinity of the materials comprising them. Their analysis suggests that the Aristarchus pyroclastic deposit is 20.75 wt.% FeO, with 58% glass and 42% agglutinate composition. The derived FeO abundance from VNIR Kaguya Multispectral Imager (MI) data (Figure 5), based on the algorithm of Lucey et al. (2000), further supports this interpretation, with FeO abundances for uncontaminated pyroclastic glass ranging from ~18 to 19.5 wt.% (Lemelin et al. 2019). Allen et al. (2012), using Diviner CF values calibrated against Apollo soil and pyroclastic glass samples, estimated the Aristarchus glass FeO content to be 19.3 ± 2.2 wt.%. The close correlation in FeO values derived from VNIR and TIR spectral modeling suggests a robust estimate for the FeO contents of the Aristarchus pyroclastic deposit glass.

The TiO_2 abundance of the pyroclastic deposit, on the other hand, is low according to multiple remote-sensing measurements. Likely due to minor errors in the optical constants used in their radiative transfer model, Wilcox et al. (2006) calculated a slightly negative value for TiO_2 abundance. The overall conclusion that the deposit is low in Ti is further supported by the low microwave loss observed in Chang'E 2 data, which is highly sensitive to the presence of ilmenite ($FeTiO_3$), although Siegler et al. (2020) noted that some pyroclastic deposits (Rimae Schröter, Bode, and Hyginus) have low microwave brightness temperature amplitudes despite high derived TiO_2 abundances from UVVIS reflectance measurements (Sato et al. 2017), likely due to the presence of Ti-bearing glass beads rather than ilmenite.

Independent TiO_2 data from the Lunar Prospector Gamma Ray Spectrometer (LP-GRS; Prettyman et al. 2006) and Neutron Spectrometer (LP-NS; Elphic et al. 2002) have a relatively large spatial footprint (~150 km), which inhibits a clean spatial isolation of the pyroclastic deposit. Even so, using

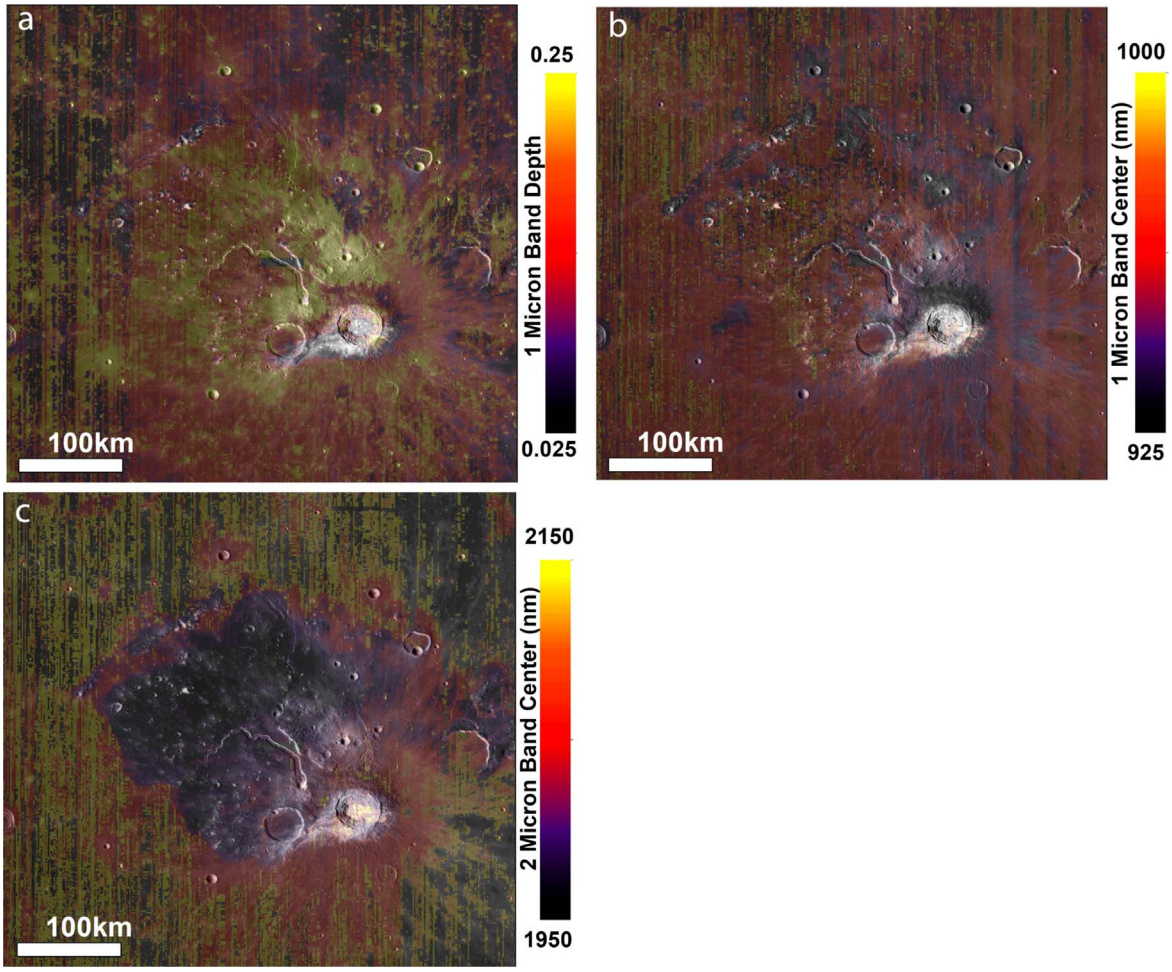

Figure 4. M^3 data covering the Aristarchus plateau and surrounding regions. All maps are overlaid on an LROC WAC mosaic. (a) 1 μm band depth. (b) 1 μm band center. (c) 2 μm band center.

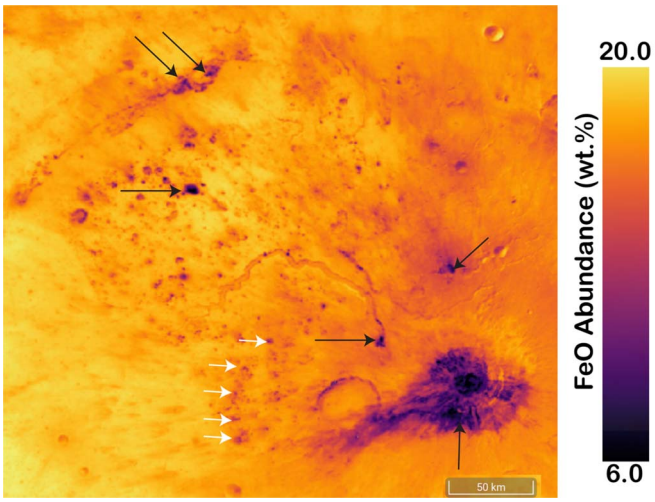

Figure 5. Kaguya MI FeO abundance (wt.%) derived from Lucey et al. (2000) overlaid on an LROC WAC mosaic (overlay and FeO values from https://quickmap.lroc.asu.edu/). Black arrows show, from top to bottom, low FeO abundances associated with Montes Agricola, Herodotus Mons, the Väisälä crater, Cobra Head, and the Aristarchus crater and its ejecta. White arrows indicate a series of knobs west of the Aristarchus crater with moderate FeO abundances.

the LP-GRS 2 degree TiO_2 map (Figure 35(a) of Prettyman et al. 2006) and the LP-NS TiO_2 map (Figure 9 of Elphic et al. 2002), we have derived average values for the Aristarchus plateau of 2.3 ± 0.3 and 1.1 ± 0.6 wt.%, respectively. Both of these values are on the lower end of the nearside TiO_2 abundances. Thus, current observations suggest that Aristarchus pyroclastic glass TiO_2 abundances are relatively low. Among Apollo lunar glass samples of presumably pyroclastic origin, the Apollo 17 orange glasses from core 74001 and their crystallized equivalents (black beads) have high Ti contents of ~9–10 wt.% (Heiken et al. 1974), at or above the high end of the LP-GRS data. Other glass types recovered at the Apollo landing sites have comparably smaller Ti abundances (Delano 1986).

In summary, multiple remote-sensing techniques reach close agreement in the FeO and TiO_2 abundances associated with Aristarchus pyroclastic glass, with FeO abundance estimates ranging from ~18 to 19.5 wt.% and TiO_2 abundances ranging from ~0 to 2 wt.%.

In addition to FeO and possible TiO_2 as components in the pyroclastic glass, the Aristarchus pyroclastic deposit contains substantial H_2O as a potential resource. Milliken & Li (2017) used M^3 3 μm band data to show that numerous pyroclastic deposits on the Moon, including that on the Aristarchus plateau, host indigenous water. Following their methods, we used data from M^3 Optical Period 2C to map the indigenous water abundance associated with the pyroclastic deposit at 280 m $pixel^{-1}$ (Figure 6). These data show that the edges of the pyroclastic deposit generally exhibit water abundances of

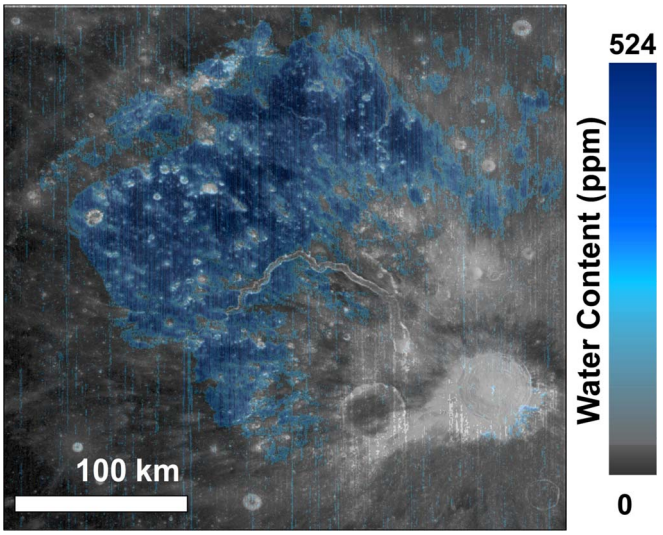

Figure 6. Water content derived from M^3 3 μm band data.

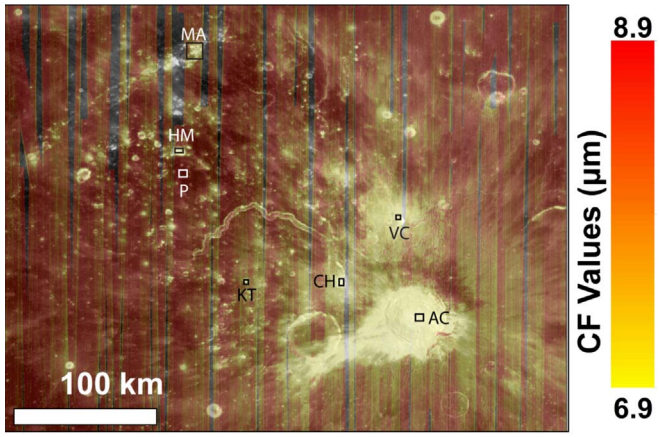

Figure 7. Diviner CF position data binned at 128 ppd and overlaid on an LROC WAC mosaic. The CF positions range from 6.9 μm (yellow), indicating silicic compositions, to 8.9 μm (red), indicating mafic compositions. Boxes and labels indicate the regions from which the spectra in Figure 12 were extracted. AC = Aristarchus crater; CH = Cobra Head; KT = knobby terrain; VC = Väisälä crater; P = pyroclastics; HM = Herodotus Mons; MA = Montes Agricola.

200–300 ppm, while the central portion of the deposit, just north of Vallis Schöteri and in the vicinity of Herodotus Mons, has water abundances in excess of 500 ppm.

The FeO map derived from Kaguya MI data (Lemelin et al. 2019) shows that the Aristarchus crater, Cobra Head, the Väisälä crater, Herodotus Mons, and portions of Montes Agricola (black arrows in Figure 5) all have exceptionally low FeO abundances (~2%–8%) compared to the Aristarchus pyroclastic deposit and surrounding mare basalts. A knobby (or hummocky) area to the west of the Herodotus crater, interpreted as remnant crater rims (Campbell et al. 2008), exhibits moderate FeO abundances (~11%–14%; white arrows in Figure 5). These areas of low FeO abundance correlate well with LRO Diviner data that indicate that these features have CF positions well shortward of typical mare, highlands, or even pure anorthosite materials (Figure 7). We note that some orbit-correlated variation in the calculated CF position is evident in the map. These variations are due to differences in the time of day and illumination conditions when the data were collected. As such, we carefully avoided clear instances of orbit-correlated CF position differences and only report CF positions and spectra for compositional anomalies associated with surface geologic features.

4.2. Silicic Regions

Based on analyses of hyperspectral M^3 VNIR data, Mustard et al. (2011) suggested that the central peak and interior of the Aristarchus crater are dominated by anorthosite, consistent with its low FeO abundance. This interpretation was in agreement with several studies of multispectral Clementine data and hyperspectral ground-based telescopic data (Lucey et al. 1986; McEwen et al. 1994; Lemouélic et al. 1999; Chevrel et al. 2009) and based on a lack of mafic 1 and 2 μm absorption features, although they noted that the M^3 data do not exhibit evidence for a 1.25 μm Fe^{2+} feature that is diagnostic of crystalline plagioclase.

Following the work of Mustard et al. (2011), we used Kaguya MI data to search for a 1.25 μm band indicative of crystalline plagioclase feldspar at the Aristarchus crater central peak and Herodotus Mons (Figure 8) and found that portions (denoted by red pixels) of each feature do indeed exhibit this band. For each MI spectrum, we removed a linear continuum defined by the values at 0.75 and 1.55 μm. Spectra with minima at 1.25 μm indicate a high abundance of an iron-bearing feldspar relative to pyroxene. With the exception of the Aristarchus crater floor, which displays a weak 1 μm band, other spots at these sites display no absorption features, suggesting (1) the presence of low-Fe plagioclase or (2) shocked plagioclase or (3) the absence of both plagioclase and mafic components. Comparison of the red pixels on the Aristarchus central peak and Herodotus Mons spectra in Figure 8 shows good agreement with other "purest anorthosite" regions on the Moon (the South Ray crater and Orientale basin rim), as well as laboratory spectra of nearly pure anorthite (Figure 8). However, the CF positions of these features, as well as the Aristarchus crater floor, which displays a weak 1 μm mafic band, are still shortward of what would be expected for the purest anorthosite regions of the Moon (e.g., Donaldson Hanna et al. 2014). This indicates that the mineral assemblages at these features must include additional components with short-wavelength CF positions that are spectrally featureless at VNIR wavelengths (e.g., quartz or other SiO_2 polymorphs).

Cheek & Pieters (2014) prepared mixtures of pyroxenes and iron-bearing plagioclase at 98 and 95 wt.% plagioclase abundances and found that at 98 wt.% plagioclase, the trace iron band is stronger than the mafic absorption near 1 μm, but the reverse was true at 95% plagioclase abundance. We therefore conclude that the ratio of feldspar to pyroxene at the Aristarchus central peak and Mons Herodotus is likely greater than 0.95. Because these locations likely contain additional silica-rich material lacking any near-IR absorption, as is suggested by the Diviner CF data, the absolute abundance of pyroxene would be lower than 5 wt. %.

Numerous studies have shown that occurrences of highly silicic, evolved lithologies on the Moon correspond closely with high Th abundances (e.g., Lawrence et al. 1999, 2003, 2007; Hagerty et al. 2006, 2009; Glotch et al. 2011; Jolliff et al. 2011). The correlation between silicic compositions and Th abundance is reflected in the geographic distribution of silicic lunar silicic features, all of which, with the exception of Compton–Belkovich, fall within the Procellarum KREEP Terrane (PKT; Jolliff et al. 2000). Of these features, among the highest concentrations of Th on the Moon occur at the Aristarchus crater (Figure 2 from

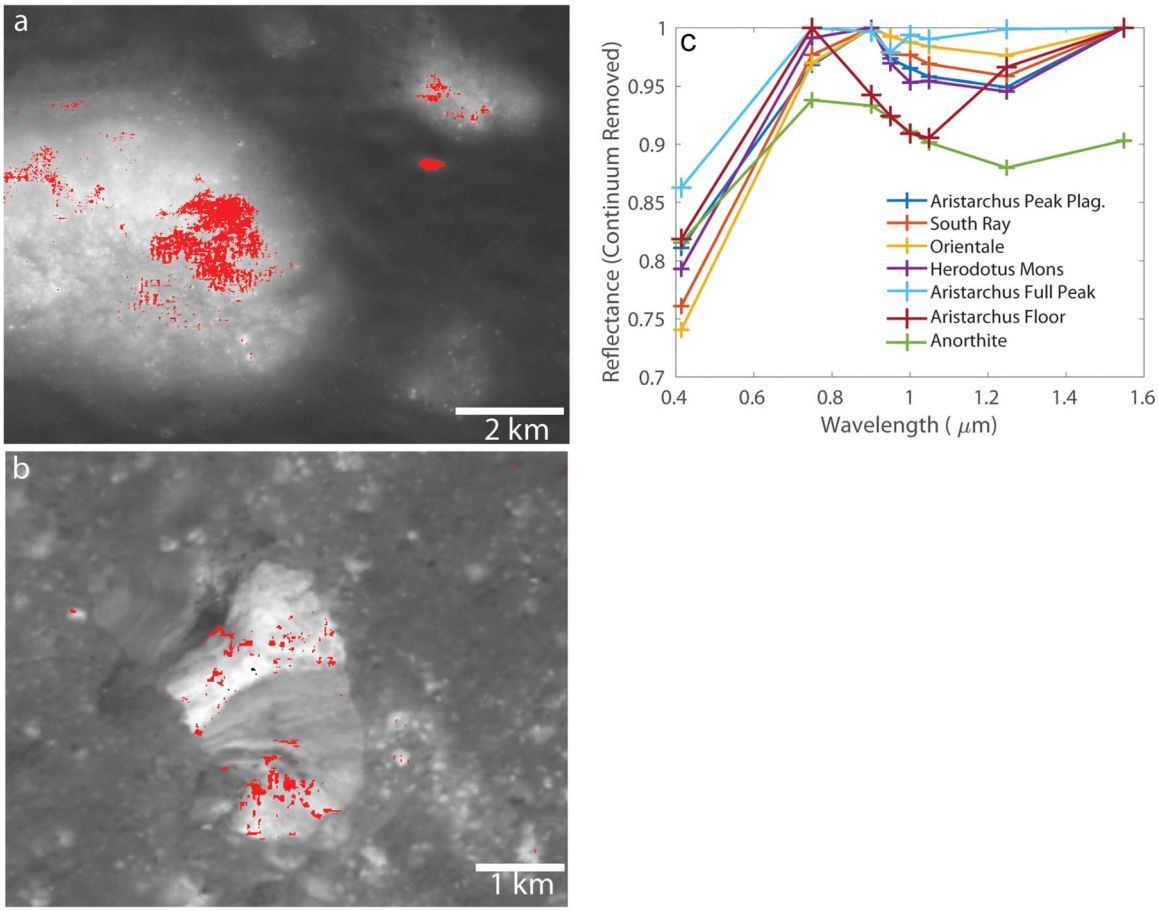

Figure 8. Kaguya MI images and spectra of silicic regions on the Aristarchus plateau. The regions of interest on Herodotus Mons and the Aristarchus crater central peak are outlined in Figure 1. (a) Kaguya MI image MI_MAP_02_N28E307N27E308SC.IMG, covering Herodotus Mons and a small unnamed nearby dome. Red pixels display a 1.25 μm feature characteristic of Fe-bearing plagioclase feldspar. (b) Kaguya MI image MI_MAP_02_N24E312N23E313SC.IMG, covering the central peak and floor of the Aristarchus crater. Red pixels display a 1.25 μm feature. (c) Average Kaguya MI spectra derived from the red pixels in panels (a) and (b). Spectra of Herodotus Mons and the Aristarchus peak are similar to the "purest anorthosite" regions of the South Ray crater and Orientale basin rim and a laboratory spectrum of anorthite from the USGS spectral library (Kokaly et al. 2017) convolved to the MI bandpasses. Average spectra for the entire Aristarchus crater central peak and the floor of the Aristarchus crater are also included.

Lawrence et al. 2000). Following Lawrence et al. (2007), we show the spatially deconvolved Th abundances for the Aristarchus plateau region (Figure 9; map from Wilson et al. 2018). The highest enhancement is associated with the Aristarchus crater and the region of the plateau immediately to north, with Th abundances up to 12 ppm. Further north, the low FeO and short-wavelength CF anomalies in portions of Montes Agricola appear to correlate with a weaker Th enrichment of ~7–8 ppm. The silicic compositions, high Th content, and geographic distribution all point to these features being the products of evolved magmas.

Each of these sites also exhibit unusually bright reflectance in LROC NAC and Wide Angle Camera (WAC) images. We use the Hapke photometrically normalized radiance factor (I/F) at 415 nm (Sato et al. 2014) as a measure of feature brightness. Typical 415 nm I/F values for the pyroclastic material on the plateau are ~0.04–0.06. Figure 10 shows a closer view using NAC image mosaics processed using ISIS3. The Aristarchus crater central peak (Figure 10(a)) has a maximum I/F of ~0.4–0.46, corresponding to the brightest portions of the NAC image. Kaguya MI FeO values for this region are <2 wt.%. The brightest portions of Cobra Head (Figure 10(b)) have I/F values of ~0.28 and FeO values of ~4 wt.%. Similarly bright material in the walls of the Väisälä crater (Figure 10(c)) exhibit I/F values of ~0.24–0.27 and FeO abundances of ~4–6 wt.%. On the northern part of the plateau, all parts of the Herodotus Mons dome (Figure 10(d)) have FeO abundances <5 wt.%, corresponding to I/F values of ~0.11–0.19, while numerous smaller domes and small craters in the area have FeO abundances in the 7–11 wt.% range, corresponding to I/F values of ~0.11–0.13. Montes Agricola is highly heterogeneous, but the brightest material (Figure 10(e)) has I/F values ranging from ~0.11 to 0.13 and FeO contents ranging from 6 to 8 wt%. Finally, the hummocky material west of the Aristarchus crater is also highly heterogeneous in LROC NAC reflectance but does exhibit some small, very bright areas. These regions correspond to I/F values of ~0.08–0.1 and FeO abundances of 7–10 wt.%.

The high LROC NAC visible reflectance and low FeO abundances for each of these sites supports the interpretation that these are at least partly composed of evolved silicic materials. We can further quantitatively evaluate the compositions of these materials using NAC photometry. As an example, following the methods of Clegg-Watkins et al. (2017), we used NAC images with a variety of illumination conditions to obtain reflectance (I/F) data for Herodotus Mons and then applied a Hapke photometric function to fit the reflectance data and determine the visible single-scattering

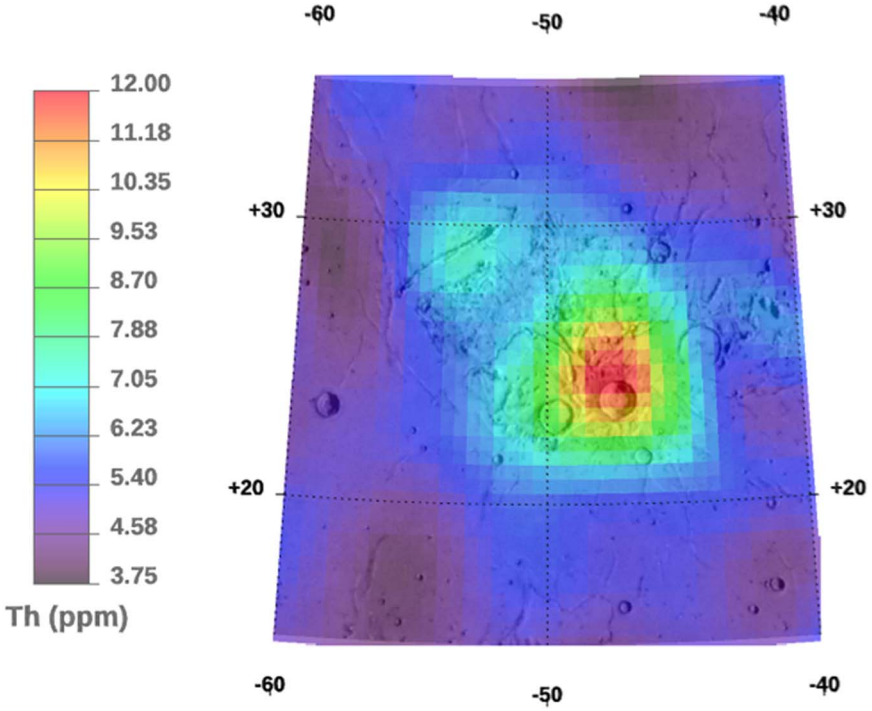

Figure 9. The Th abundances (ppm) derived from the LP-GRS (Wilson et al. 2018).

albedo (w) for a flat area near the top of the mound. Single-scattering albedo is dependent on composition and mineralogy, and for the Moon, it increases with increasing feldspathic composition and reflectance. The flat area on top of Herodotus Mons has a w value of 0.55, which is similar to other silicic features on the Moon, including the CBVC (0.53–0.66), Hansteen Alpha (0.4–0.62), and Aristarchus ejecta (0.53). Similarly, we used Hapke photometric modeling and phase curves to determine the I/F at a common 30° phase angle to compare Herodotus Mons with analyses of other silicic features. This process gives an $I/F(30°)$ of 0.12 for Herodotus Mons, which is similar to values found for the CBVC (0.14–0.20), Hansteen Alpha (0.09–0.17), and Aristarchus ejecta (0.099; Clegg-Watkins et al. 2017). The high reflectance and w of the values at these sites, when coupled with Diviner data and correlated with mafic mineralogy from Apollo samples, support the interpretation that they contain felsic lithologies. The lower w values for Herodotus Mons and Hansteen Alpha may indicate mixing of felsic components with the surrounding basalt or intermediate silicic compositions, such as trachyandesite or trachyte (Clegg-Watkins et al. 2017).

To further constrain the compositions of these features, we can examine their Diviner three-point TIR emission spectra and compare with the laboratory spectra of mare and highlands simulants and terrestrial rhyolite collected in a simulated lunar environment. Figure 11 shows the TIR spectra of highlands (LHS-1) and mare (LMS-1) lunar regolith simulants (University of Central Florida Exolith Lab, https://sciences.ucf.edu/class/exolithlab/) and a rhyolite from Castle Rock, Colorado, USA, collected in the Planetary and Asteroid Regolith Spectroscopy Environment Chamber (PARSEC) at Stony Brook University using the methods of Shirley & Glotch (2019). Spectra of the LMS-1 and LHS-1 simulants were measured as they were delivered without any further processing. LMS-1 has a size range of 0.04–300 μm, with a mean grain size of 45 μm. LHS-1 has a size range of 0.04–400 μm, with a mean grain size of 50 μm. The rhyolite sample was sieved to a size fraction of 32–64 μm.

The chemical compositions of the rhyolite, LHS-1, and LMS-1 simulants, measured by X-ray fluorescence, are shown in Table 1. The simulants were chosen to represent average lunar mare and highlands and provide a direct comparison of their TIR spectral features to our rhyolite sample. The LMS-1 mare simulant is not primarily glass, as the Aristarchus pyroclastic deposit likely is, but it is a reasonable analog for the pyroclastic deposit in the CF region, which is sensitive to overall SiO_2 abundance and not crystallinity (Shirley et al. 2019).

The CF position of the rhyolite (1344 cm^{-1}; 7.44 μm) lies well shortward of the CF positions of both the mare (1222 cm^{-1}; 8.13 μm) and highlands (1244 cm^{-1}; 8.03 μm) simulants. The measured CF positions of the mare and highlands simulants are at shorter wavelengths than typically seen on the Moon (Greenhagen et al. 2010). Diviner primarily measures emission from mature lunar soils, and space weathering is known to shift CF positions to longer wavelengths (Glotch et al. 2015; Lucey et al. 2017).

When convolved to Diviner spectral sampling (Figure 12(a)), the rhyolite exhibits a concave-up spectral shape in the three-point spectrum, while both the highlands and mare simulants show more typical spectral signatures identified by Diviner (e.g., Greenhagen et al. 2010). The vast majority of the plateau north of Vallis Schröteri exhibits a Diviner three-point spectrum similar to the LMS-1 simulant. This is consistent with the dominant VNIR spectral signature of pyroclastic glass of basaltic composition. At Diviner spectral sampling, we would not expect to see any spectral difference between crystalline and glassy materials of roughly the same composition.

The Diviner three-point spectra of the silicic features on the plateau are more similar to the convolved rhyolite spectrum than either the mare or highlands simulants (Figure 12(b)). Despite having a spectral character that is markedly different from the Aristarchus pyroclastic materials and the laboratory spectra of the highlands and mare simulant, the spectra of the

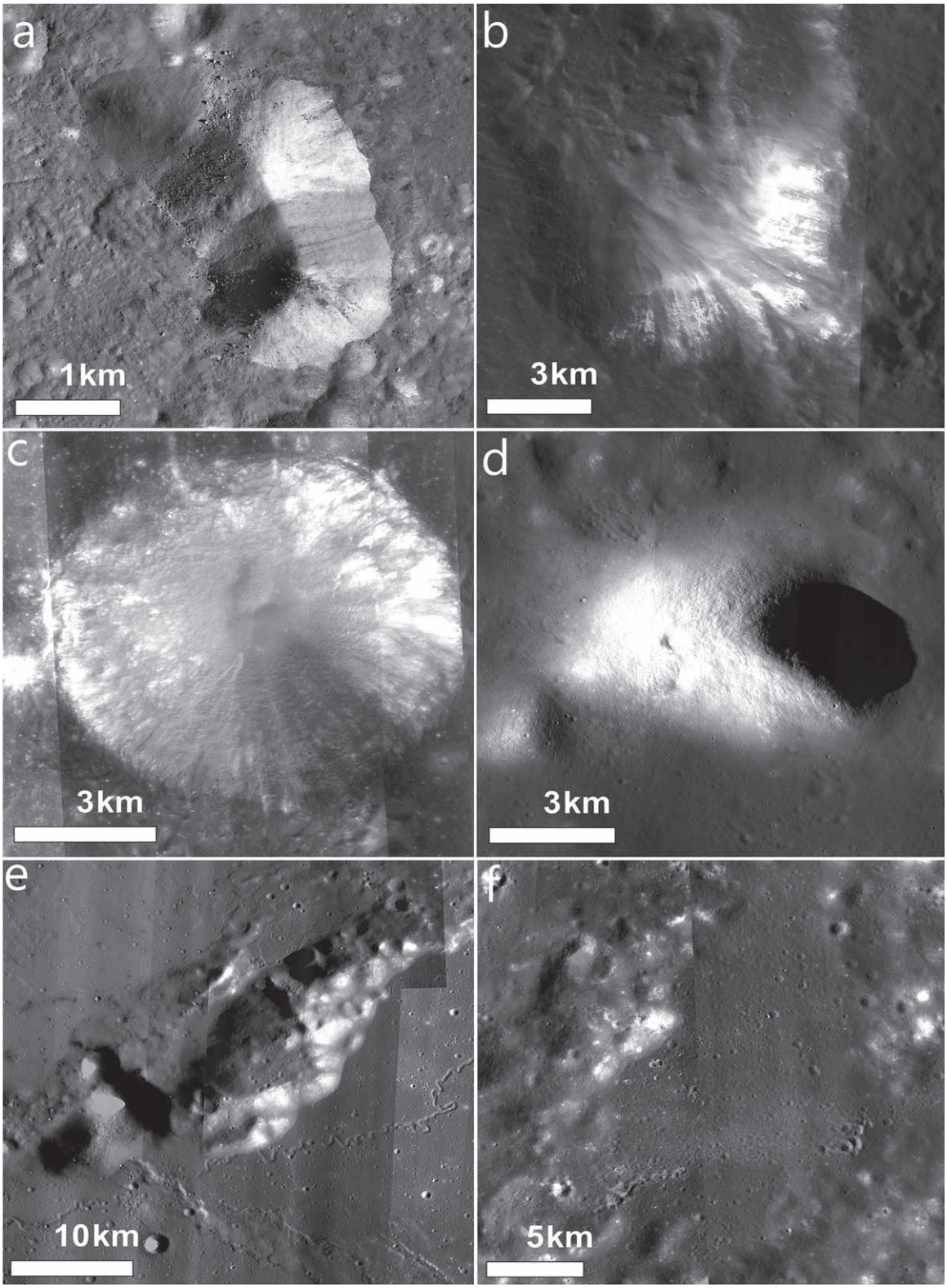

Figure 10. LROC NAC frames covering regions of suspected silicic composition. North is up in each frame. (a) Aristarchus crater central peak. (b) Cobra Head. (c) Väisälä crater. (d) Herodotus Mons. (e) Montes Agricola. (f) Hummocky terrain west of Aristarchus. Image locations are shown in Figure 1.

silicic features, with the exception of Herodotus Mons, have only very slightly concave-up or even concave-down spectra. This may be due to one of several factors: (1) the silicic features identified here have a more intermediate composition than the rhyolite measured in the lab, (2) space weathering has shifted the CFs of these features to longer wavelengths, or (3) Diviner is sampling mixtures of silicic and mafic materials within its ∼500 m field of view.

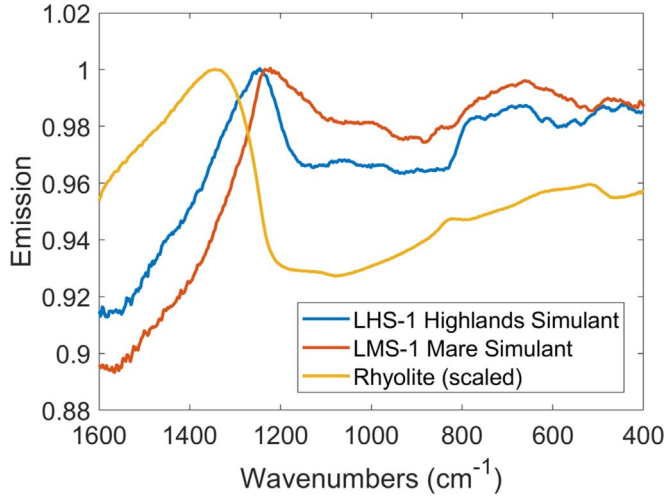

Figure 11. Thermal emission spectra of lunar soil simulants and particulate rhyolite acquired in a simulated lunar environment.

Table 1
Major Element Chemistry (wt.%) of Rhyolite, LMS-1, and LHS-1

Oxide	Rhyolite	LHS-1[a]	LMS-1[a]
SiO_2	71.69	48.1	40.2
Al_2O_3	14.1	25.8	14.0
K_2O	7.63	0.7	0.6
Na_2O	3.43	…	…
Fe_2O_3	1.46	3.7	13.9
CaO	0.823	18.4	9.8
TiO_2	0.456	1.1	7.3
MgO	0.143	0.3	12.0
P_2O_5	0.071	1.0	1.0

Note.
[a] Chemistry for LHS-1 and LMS-1 simulants reported at https://exolithsimulants.com/collections/regolith-simulants/.

5. Mission and Notional Payload Overview

5.1. Science Motivation

A mission to the Aristarchus plateau would be driven by several important questions. These include, but are not limited to, the following. (1) How are large-scale granitic/rhyolitic compositional features on the Moon generated in the absence of plate tectonics? Do they reflect hot-spot processes as seen on Earth? (2) Is there any field evidence for a relationship between the basaltic and silicic materials? What petrologic processes would indicate that they could or could not be related, and what do these inferences imply about the lunar interior? (3) Is there a gradation in silicic compositions that is not discernible from orbit due to limited spectral and/or spatial resolution? What lithologies are represented by the silicic material (e.g., trachytes, syenite, potassic granite, potassic rhyolite)? Are there intermediate compositions? (4) What do the correlations between SiO_2 content, Th, and/or H_2O tell us about lunar interior composition and evolution? (5) Are there coatings on the pyroclastic materials that can tell us about volatiles (other than H_2O) in the lunar interior? (6) How do the compositions of the pyroclastic materials and basaltic lava flows in the region differ, and can they be related? Each of these questions could be addressed through analyses of pyroclastic, basaltic, and silicic materials on the Aristarchus plateau by one or more missions.

5.2. Suggested Payload Overview

Given the dual goals of characterizing material from the largest pyroclastic deposit on the Moon and characterizing compositionally evolved silicic rocks, we suggest that any landed mission to the Aristarchus plateau should include a core science payload of a TIR hyperspectral imager and a GRNS. A panchromatic or multispectral imager for context imaging would also be required, and, depending on the size and scope of the mission, it would be useful to comanifest this payload with a hyperspectral VNIR point spectrometer or imager for characterization of mafic mineral/glass content and H_2O associated with the pyroclastic deposit.

A remote-sensing TIR instrument would provide hyperspectral TIR images with 10 cm^{-1} spectral sampling of the landing site and surrounding terrain, preferably over the ~5.5–15 μm wavelength range. From these data, it would be possible to calculate the bulk mineralogy of the silicic and any other materials at the landing site, which we have been unable to do with Diviner remote-sensing data due to its limited spectral and spatial resolution. The hyperspectral data set would enable us to perform spectral mixture analysis and determine the relative proportions of crystalline silica phases (e.g., quartz, tridymite, cristobalite), glass, plagioclase, and alkali feldspar associated with silicic rocks, as well as glassy and crystalline mafic phases that may constitute the pyroclastic deposit. These measurements would allow us to directly compare the modal mineralogy of the silicic and pyroclastic materials at the landing site to those in the Apollo sample collection. This type of quantitative analysis is not possible with single-band or multispectral infrared measurements.

The warmest surface temperatures (~350–375 K at the Aristarchus plateau) during the lunar day (e.g., Vasavada et al. 2012; Williams et al. 2017) would provide substantial signal to enable high-quality thermal emission measurements with total measurement times of seconds or minutes for small scans or hours for large panoramas. Rover-based TIR remote sensing has demonstrated success in identifying unique lithologies and quantifying rock and soil mineralogy on Mars (e.g., Christensen et al. 2004; Glotch et al. 2006; Glotch & Bandfield 2006; Ruff et al. 2006; Rogers & Aharonson 2008; Ruff & Hamilton 2017).

The GRNS would be a compact system that uses a scintillator-based gamma-ray spectrometer (GRS; Peplowski et al. 2014) and an ^{3}He sensor-based neutron spectrometer (NS). The GRS would measure gamma rays with energies from 300 keV to 9 MeV and quantify abundances for the major rock-forming elements (e.g., Mg, Si, Al, Ca, Ti, Fe), as well as various radioactive trace elements (e.g., K, Th, U). The NS would use two separate sensors to measure thermal and epithermal neutrons, from which hydrogen (Feldman et al. 1998) and neutron-absorbing elements (Elphic et al. 2000) can be measured. The minimum measurement time for obtaining GRNS measurements is on the order of a few hours for gamma-ray data and tens of minutes for neutron data. The spatial resolution provided by these data is approximately the height of the sensor above the surface. The GRNS data would therefore be used to determine the major- and trace-element concentrations of pyroclastic and silicic materials at the landing site, including Th. These mineralogic and major-/trace-element abundances could be directly compared to the silicic Apollo samples to determine how representative the Apollo sample suite

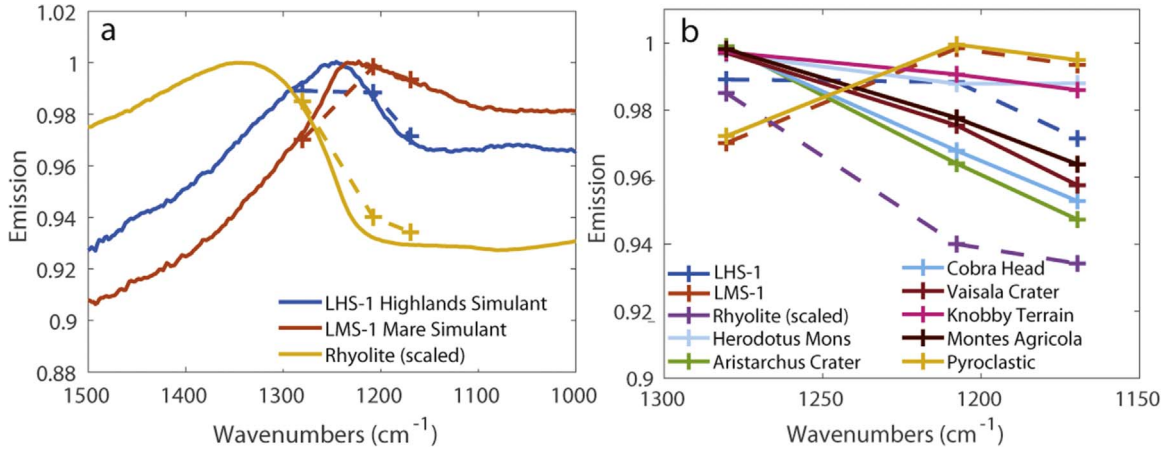

Figure 12. (a) Laboratory spectra (solid lines) and their equivalents convolved to the Diviner filter functions (dashed lines). (b) Convolved laboratory spectra (dashed lines) and Diviner three-point spectra of several units on the Aristarchus plateau.

is of silicic materials on the Moon. This instrument suite would also be capable of determining the hydration state of the landing site materials through TIR measurement of the 6 μm H_2O fundamental vibrational band (Honniball et al. 2020) and the GRNS epithermal neutron count rate, which provides a measure of water equivalent hydrogen concentration (Feldman et al. 1998). While not yet demonstrated in space, rover-based passive measurements of hydrogen content via neutron counting have been comprehensively demonstrated with Earth-based measurements (Elphic et al. 2015) and are planned for multiple future lunar missions (e.g., Colaprete et al. 2021).

5.3. Possible Mission Profiles

Clearly, the level of science that could be performed at a potential Aristarchus landing site will depend on the mission profile and instrumentation available. One of the first NASA CLPS missions, operated by Intuitive Machines, is scheduled to land near Vallis Schröteri in 2021 (Martin 2019). However, the landing site and scientific payload are not designed to address questions related to lunar volcanism or mineralogical and chemical characterization of the Aristarchus plateau materials. A later CLPS mission on a static lander to one of our proposed landing sites (detailed below) would offer the opportunity to interrogate multiple lithologies via landed remote-sensing measurements. The scientific return of the mission would be further enhanced by mobility capability, enabling high spatial resolution measurements of both silicic and pyroclastic materials by both the TIR hyperspectral imager and GRNS.

Potentially transformational science would be enabled by a sample return capability, although mobility capability would be highly desirable for careful selection of samples to be returned to Earth. Sampling strategies and the characteristics of returned samples can vary considerably depending on the mission profile and scientific goals. The Chinese Chang'e-5 mission returned 1.73 kg of samples from young basalts in the PKT by employing a static lander using a shovel and drill (Lin et al. 2021). This strategy was appropriate for the mission's scientific goals, which included dating young basalts near the Mons Rümker volcanic complex (Zhao et al. 2017) and determining their volatile and trace-element concentrations to characterize the mantle source of these materials. A similar strategy could be employed at the Aristarchus plateau given a suitably homogeneous landing site on the floor of the Aristarchus crater or on the pyroclastic deposit. A more complex sampling strategy has been developed for the proposed MoonRise mission to the South Pole–Aiken basin. Samples would be collected from a static lander and include >1 kg of unprocessed soil and a sample sieved to increase the concentration of small rock fragments, which would have the greatest likelihood of increasing the compositional diversity of the returned sample (Jolliff et al. 2010). A similar sample return strategy would work best at a site most likely to have compositional diversity, such as on or near the ejecta blanket of the Aristarchus crater or the boundary between the pyroclastic deposit and Herodotus Mons.

The complex geology of the Aristarchus region would be best characterized by human astronauts with geologic training. The Artemis-returned sample mass will be in the tens of kilograms, enabling the collection of bulk regolith samples and pebbles and rocks carefully selected by astronauts (Artemis Science Definition Team Report). Given the complexity and ISRU value of the region, Aristarchus should be considered as a potential site for the first nonpolar crewed Artemis mission. The value of human exploration is clearly demonstrated by the Apollo 17 mission to the Taurus–Littrow valley on the boundary between Mare Serenetatis and anorthositic highlands. Taurus–Littrow exhibits a complex stratigraphy of Imbrian-aged ejecta, lava flows, and pyroclastic deposits, providing some first-order similarities to the Aristarchus plateau. Our understanding of the geology of the region was greatly enhanced through careful field work and sample selection by the Apollo 17 crew, which has provided a basis for later remote-sensing investigations and the development of arguments for future crewed missions to the region (Schmitt et al. 2017). The samples returned from Apollo 17 also provided major insight into explosive eruptions and pyroclastic deposits on the Moon (e.g., Weitz et al. 1998). Maximizing our understanding of the diverse magmatic history of the Aristarchus region requires a similar but more extended crewed field investigation.

5.3.1. Aristarchus Crater Landing Site

The diversity and scales of geologic structures at the Aristarchus plateau demand a sustained multimission exploration program. The volcanic materials on the plateau represent

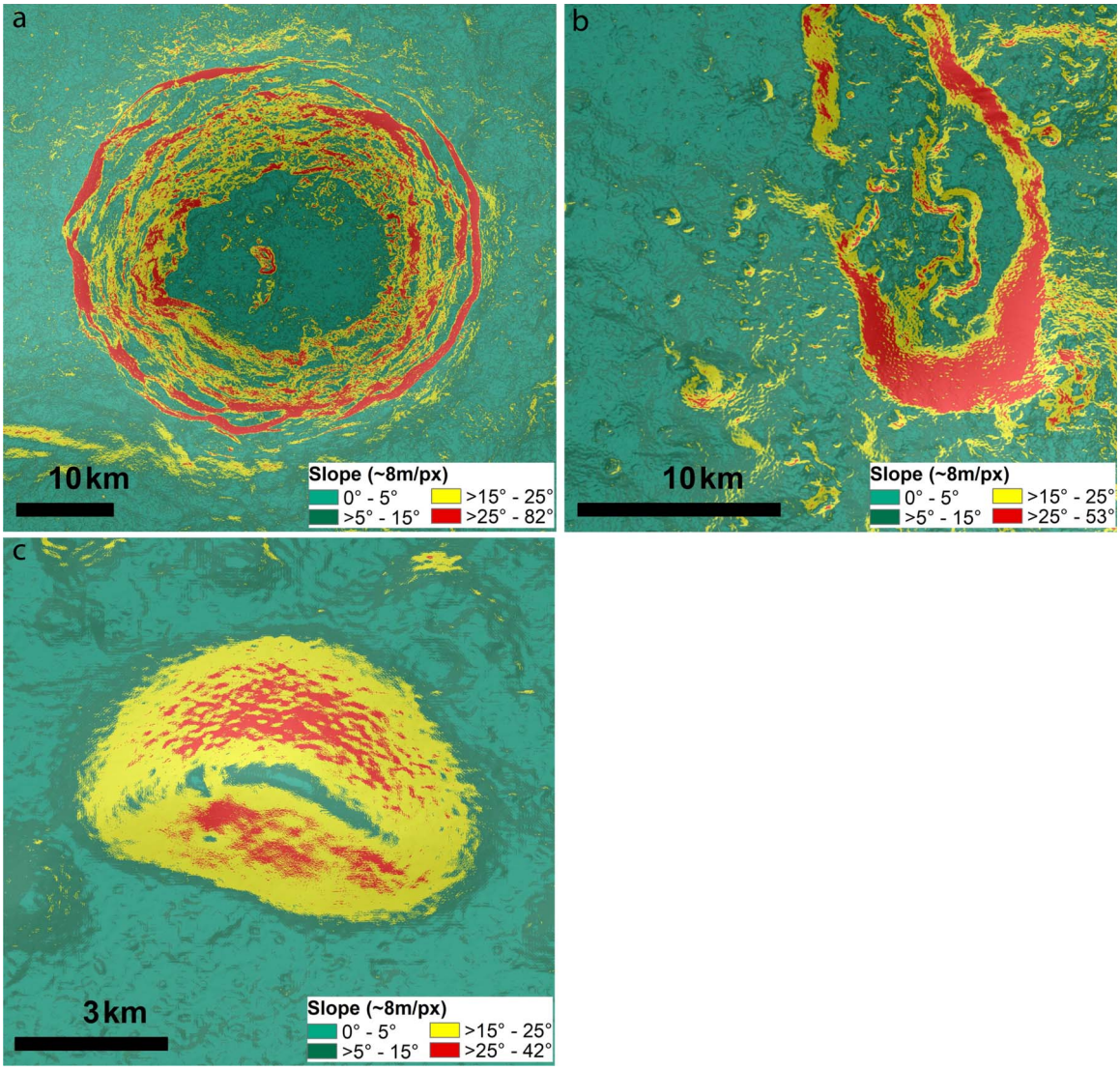

Figure 13. Slopes derived from the high-resolution (8 m pixel^{-1}) SELENE (Kaguya) stereo DEM overlaid on its hillshade map. (a) Aristarchus crater. (b) Cobra Head. (c) Herodotus Mons.

extremes in volcanic style and composition (basaltic Hawaiian-style fire fountain pyroclastic eruptions and silicic volcanism). At least two silicic features on the plateau should be visited. The central peak and ejecta of the Aristarchus crater appear to have excavated a vast granitic pluton. Diviner CF and LP-GRS Th data strongly indicate an evolved composition, while M^3 and Kaguya MI data do not display strong mafic absorptions associated with the central peak and interior of the crater or over most of the ejecta. However, mafic materials, including olivine, were excavated by the impact and are present in portions of the ejecta blanket (Chevrel et al. 2009, 2017; Mustard et al. 2011; Arnold et al. 2016). These features demonstrate substantial subsurface compositional complexity and heterogeneity in the region. In situ analysis of the interior of the Aristarchus crater or its granitic (or syenitic) ejecta would enable direct comparison of lunar rocks with a likely silicic composition with granitic clasts in the Apollo sample collection. The crater interior and much of the ejecta blanket are compositionally uniform at the Diviner and M^3 pixel scales (<500 m pixel^{-1}), suggesting that science at this site could be accomplished with a landed mission with little or no mobility. While the central peak of the crater would likely be off-limits to a lander due to hazardous slopes (Figure 13), much of the crater floor, in particular the region to the east of the central peak, exhibits slopes of only 1°–5° in high resolution derived from the SELENE (Kaguya) stereo DEM (Haruyama et al. 2012).

5.3.2. Cobra Head Landing Site

Cobra Head (Figure 10(b)) represents a possible site of bimodal volcanism on the plateau. It is the source region of Vallis Schröteri, the largest sinuous rille on the Moon, which was likely carved by thermal erosion of the plateau surface by low-viscosity mafic lava (Hurwitz et al. 2013). However, Cobra Head also includes outcrops of bright material in LROC NAC images that display low CF values consistent with a silicic composition (Figure 7) and low FeO abundances between 4 and 7 wt.% (Figure 5). Thus, a mission to Cobra Head would enable exploration of both basaltic and silicic volcanism on the Moon and potentially sample the transition between the two eruptive styles. While Cobra Head is relatively close to the Aristarchus crater (~30 km from the western crater rim), it exhibits clear evidence for an extrusive, rather than intrusive,

silicic lithology. This evidence includes the Cobra Head vent's occurrence on a rough-textured cone ~50–60 km in diameter, presumably constructed from high effusion rate basaltic (and potentially silicic) lavas, and the presence of Vallis Schröteri itself, as well as a smaller nested rille within it (Hurwitz et al. 2013; Head & Wilson 2017). A direct comparison between the likely intrusive silicic rocks associated with the Aristarchus crater and the extrusive volcanic rocks of Cobra Head could further expand our understanding of the formation of evolved rocks on the Moon. The large slopes (~25°–53°; Figure 13(b)) associated with bright deposits in the wall of Cobra Head may make exploration of the region a challenge. It is unlikely that the goals of interrogating both silicic and basaltic materials could be accomplished with a static lander. Therefore, a mission to Cobra Head would likely require a platform with mobility and the capability to traverse the steep slopes at the site.

5.3.3. Herodotus Mons Landing Site

A potentially ideal landing site is in the vicinity of Herodotus Mons (Figure 10(d)), offering a safe landing site and the opportunity to sample both silicic and pyroclastic materials with up to 500 ppm H_2O without the potential ambiguity of origin from analyzing a region heavily contaminated by impact ejecta adjacent to the Aristarchus crater. Surfaces in the pyroclastic deposit immediately south of Herodotus Mons have slopes ranging between ~1° and 6° (Figure 13(c)), while the small silicic dome immediately adjacent to Herodotus Mons to the southwest has maximum slopes of 14°. Herodotus Mons itself has maximum slopes of ~28° over parts of the dome, although silicic areas at the base tend to have more modest slopes of ~15°–20°. For a mission with mobility capability, trafficability on the pyroclastic deposit is not likely to be a concern. Bickel et al. (2019) conducted a detailed study of boulder tracks on pyroclastic deposits to calculate their bearing capacity, or ability to bear a load and provide traction for motion (Bekker 1960; Carrier et al. 1991). They found that the bearing capacities of the pyroclastic deposits they investigated are statistically equal to or significantly higher than known values for mare and highlands surfaces.

Herodotus Mons and several smaller domes and craters all exhibit Kaguya MI FeO abundances of 4–7 wt.%. Herodotus Mons has the strongest signature of silicic composition in Diviner CF data on the Aristarchus plateau. As with Cobra Head, a Herodotus Mons landing site would provide the opportunity to examine extrusive silicic rocks on the plateau and provide a direct contrast to the likely intrusive silicic rocks exposed by the Aristarchus crater. Furthermore, the pyroclastic deposit surrounding Herodotus Mons provides a flat, safe landing site for a potential mission. A mission to Herodotus Mons would strongly benefit from mobility, and it offers the most compelling target on the plateau for a potential sample return mission. In situ and Earth-based characterization of silicic rocks from Herodotus Mons would provide an opportunity to constrain the origin of materials that are rare in the Apollo sample collection. Furthermore, pyroclastic materials sourced from deep, primitive, gas-rich magmas, coupled with their abundance of metals, oxides, and volatiles, are among the highest priority from both a scientific and exploration perspective. The return of these samples to Earth would provide a new data set with which to probe the primitive lunar interior.

6. Discussion and Conclusions

Of the identified silicic features on the Moon, Aristarchus appears to be unique in that the silicic materials exposed by the Aristarchus crater suggest the presence of a large subsurface silicic pluton (Glotch et al. 2010). While the central peak and interior of the Aristarchus crater are clearly silicic based on the lack of VNIR mafic mineral absorption features and a diagnostic Diviner spectral signature, portions of the rays southeast of the crater display a diagnostic 1 μm olivine feature and are enriched in orthopyroxene with absorptions at 1 and 2 μm (Mustard et al. 2011). This olivine detection was later confirmed by analyses of Diviner Lunar Radiometer data (Arnold et al. 2016). Thus, there appears to be a gradation between mafic-free silicic material, noritic rock assemblages, and olivine-bearing rocks exposed by the Aristarchus impact. This suggests a highly heterogenous and unusual subsurface mineral assemblage.

Two hypotheses have been proposed for the formation of highly silicic, evolved compositions on the Moon. Silicate liquid immiscibility (SLI) involves extreme fractional crystallization of melts resulting in two immiscible liquids, one of which is FeO-poor and one of which is FeO-rich. Clear textural evidence of this process has been seen in felsite clasts in the Apollo sample collection (Jolliff et al. 1999). However, the small amount of residual melt left over at the end of this process likely cannot explain the diversity and spatial extent of silicic features found on the Aristarchus plateau. Hagerty et al. (2006) proposed basaltic underplating as a mechanism for the formation of silicic melts. In this scenario, basaltic magma intrudes into anorthositic crust, melting it, and, through additional fractional crystallization, produces silicic melts. This process is capable of producing large volumes of rhyolitic melts (Maaløe & McBirney 1997). It also, however, places significant compositional constraints on the felsic rocks that can be produced, and it is not clear that this process could produce the unusual juxtaposition of silica- and olivine-rich rocks found in the interior, rim, and ejecta of the Aristarchus crater.

It has long been suggested that the Aristarchus plateau is a large highlands block that was displaced and uplifted by the Imbrium impact event (Zisk et al. 1977; Wilhelms 1987). Furthermore, the plateau falls within the PKT (Jolliff et al. 2000) and is a Th hot spot. The combination of anorthositic crust and a high abundance of heat-producing elements appears to favor the basaltic underplating mechanism, which can produce voluminous silicic melts. Clearly, basaltic magmas also reached the surface, leading to the formation of the numerous sinuous rilles on the plateau and the vast pyroclastic deposit mantling all of the volcanic features on the plateau. It is possible that the basaltic underplating and SLI mechanisms both operated beneath the Aristarchus crater, producing the observed mafic/felsic assemblage. To date, similar silicic/olivine-rich assemblages have not been found at other sites on the Aristarchus plateau.

A series of missions to the Aristarchus plateau offers the opportunity to address numerous questions related to the generation and evolution of silicic magmas, their relationship to basaltic volcanism, and their expression on the lunar surface. A mission to the Aristarchus crater floor or silicic ejecta would offer the opportunity to sample likely plutonic silicic rocks. A landed mission in the vicinity of Herodotus Mons would characterize both silicic and pyroclastic material. Such missions

should include, at a minimum, (1) a TIR hyperspectral imager to characterize the mineralogy, glass, and water content of silicic and pyroclastic deposits and (2) a GRNS to characterize the major- and trace-element chemistry of silicic and pyroclastic deposits and the water equivalent hydrogen concentration of the deposits. The science returned from this instrument suite would be augmented by a VNIR hyperspectral point spectrometer and imager. Together, these measurements would provide a new framework with which to evaluate a diverse range of lunar volcanic processes.

We thank the two anonymous reviewers for their helpful suggestions that improved the content and clarity of this manuscript. This work was funded by the Lunar Reconnaissance Orbiter Extended Science Mission 4 and the RISE2 node of NASA's Solar System Exploration Research Virtual Institute (PI: T.D. Glotch).

ORCID iDs

Timothy D. Glotch https://orcid.org/0000-0002-8187-3609
David J. Lawrence https://orcid.org/0000-0002-7696-6667

References

Allen, C. C., Greenhagen, B. T., Donaldson Hanna, K. L., & Paige, D. A. 2012, JGRE, 117, E00H28
Allen, C. C., Morris, R. V., & McKay, D. S. 1996, JGR, 101, 26085
Artemis III Science Definition Team Report, NASA Special Paper 20205009602, https://www.nasa.gov/sites/default/files/atoms/files/artemis-iii-science-definition-report-12042020c.pdf
Arnold, J. A., Glotch, T. D., Lucey, P. G., et al. 2016, JGRE, 121, 1342
Ashley, J., Robinson, M. S., Stopar, J. D., et al. 2016, Icar, 273, 248
Barker, M. K., Mazarico, E., Neumann, G. A., et al. 2016, Icar, 273, 346
Bekker, M. G. 1960, Off-the-road Locomotion: Research and Development in Terramechanics (Ann Arbor, MI: Univ. Michigan Press)
Bickel, V. T., Honniball, C. I., Martinez, S. N., et al. 2019, JGRE, 124, 1296
Boyce, J. M., Giguere, T., Mouginis-Mark, P., Glotch, T., & Taylor, G. J. 2018, P&SS, 162, 62
Boyce, J. M., Giguere, T. A., Hawke, B. R., et al. 2017, Icar, 283, 254
Braden, S. E., Stopar, J. D., Robinson, M. S., et al. 2014, NatGe, 7, 787
Campbell, B. A., Carter, L. M., Hawke, B. R., Campbell, D. B., & Ghent, R. R. 2008, Geo, 36, 135
Carrier, W., III., Olhoeft, G. R., & Mendell, W. 1991, in Lunar Source Book, ed. G. H. Heiken, D. T. Vaniman, & B. M. French (Cambridge: Cambridge Univ. Press), 475
Cheek, L. C., & Pieters, C. M. 2014, AmMin, 99, 1871
Chevrel, S. D., Pinet, P. C., Daydou, Y., et al. 2009, Icar, 199, 9
Chevrel, S. D., Pinet, P. C., & Daydou, Y. 2017, LPSC, 48, 1907
Chevrel, S. D., Pinet, P. C., & Head, J. W., III 1999, JGR, 104, 16515
Christensen, P. R., Ruff, S. W., Fergason, R. L., et al. 2004, Sci, 305, 837
Clegg-Watkins, R. N., Jolliff, B. L., Watkins, M. J., et al. 2017, Icar, 285, 169
Colaprete, A., Elphic, R. C., Shirley, M., et al. 2021, LPSC, 52, 1523
Conel, J. E. 1969, JGR, 74, 1614
Coombs, C. R., Hawke, B. R., & Allen, C. C. 1998, in Space 98, ed. R. G. Galloway & S. Lokaj (New York: Am. Soc. of Civ. Eng.), 608
Delano, J. W. 1986, LPSC, 16, D201
Delano, J. W., & Livi, K. 1981, LPSC, 12, 226
Donaldson Hanna, K. L., Cheek, L. C., Pieters, C. M., et al. 2014, JGRE, 119, 1516
Elphic, R. C., Heldmann, J. L., Marinova, M. M., et al. 2015, AdSpR, 55, 2438
Elphic, R. C., Lawrence, D. J., Feldman, W. C., et al. 2000, JGR, 105, 20333
Elphic, R. C., Lawrence, D. J., Feldman, W. C., et al. 2002, JGRE, 107, 5024
Feldman, W. C., Maurice, S., Binder, A. B., et al. 1998, Sci, 281, 1496
Gaddis, L. R., Pieters, C. M., & Hawke, B. R. 1985, Icar, 61, 461
Gaddis, L. R., Staid, M. I., Tyburczy, J. A., Hawke, B. R., & Petro, N. E. 2003, Icar, 161, 262
Glotch, T. D., & Bandfield, J. L. 2006, JGRE, 111, E12S06
Glotch, T. D., Bandfield, J. L., Christensen, P. R., et al. 2006, JGRE, 111, E12S03
Glotch, T. D., Bandfield, J. L., Lucey, P. G., et al. 2015, NatCo, 6, 6189
Glotch, T. D., Hagerty, J. J., Lucey, P. G., et al. 2011, GeoRL, 38, L21204
Glotch, T. D., Lucey, P. G., Bandfield, J. L., et al. 2010, Sci, 329, 1510
Glotch, T. D., Shirley, K. A., & Greenhagen, B. T. 2017, LPSC, 48, 1688
Green, R. O., Pieters, C., Mouroulis, P., et al. 2011, JGRE, 116, E00G19
Greenhagen, B. T., Lucey, P. G., Wyatt, M. B., et al. 2010, Sci, 329, 1507
Gustafson, J. O., Bell, J. F., Gaddis, L. R., Hawke, B. R., & Giguere, T. A. 2012, JGRE, 117, E00H25
Hagerty, J. J., Lawrence, D. J., Hawke, B. R., et al. 2006, JGR, 111, E06002
Hagerty, J. J., Lawrence, D. J., Hawke, B. R., & Gaddis, L. R. 2009, JGR, 114, E04002
Hapke, B. 1981, JGR, 86, 3039
Hapke, B. 1993, Theory of Emittance and Reflectance Spectroscopy (New York: Cambridge Univ. Press)
Hapke, B. 2001, JGR, 106, 10039
Haruyama, J., Hara, S., Kazuyuki, H., et al. 2012, LPSC, 43, 1200
Head, J. W., III, & Hess, P. C. 1978, LPSC, 9, 488
Head, J. W., III, & McCord, T. B. 1978, Sci, 199, 1433
Head, J. W., III, & Wilson, L. 1981, LPSC, 12, 427
Head, J. W., III, & Wilson, L. 2017, Icar, 283, 176
Heiken, G. H., McKay, D. S, & Brown, R.W 1974, GeCoA, 38, 1703
Hevelius, J. 1647, Selenographia, Sive Lune Discriptio (Gdańsk: Andreas Hünefeld)
Hiesinger, H., Head, J. W., III, Wolf, U., Jaumann, R., & Neukum, G. 2011, GSA Special Papers, Vol. 477, Recent Advances and Current Research Issues in Lunar Stratigraphy (Boulder, CO: Geological Soc. of America), 477
Honniball, C. I., Lucey, P. G., Li, S., et al. 2020, NatAst, 5, 121
Hurwitz, D. M., Head, J. W., & Hiesinger, H. 2013, P&SS, 79, 1
Jawin, E. R., Valencia, S. N., Watkins, R. N., et al. 2019, E&SS, 6, 2
Jolliff, B. L., Alkalai, L., Pieters, C. M., et al. 2010, LPSC, 41, 2450
Jolliff, B. L., Floss, C., McCallum, I. S., & Schwartz, J. M. 1999, AmMin, 84, 821
Jolliff, B. L., Gillis, J. J., Haskin, L., et al. 2000, JGR, 105, 4197
Jolliff, B. L., Wiseman, S. A., Lawrence, S. J., et al. 2011, NatGe, 4, 566
Klima, R. L., Dyar, M. D., & Pieters, C. M. 2011, M&PS, 46, 379
Klima, R. L., Pieters, C. M., & Dyar, M. D. 2007, M&PS, 42, 235
Kokaly, R. F., Clark, R. N., Swayze, G. A., et al. 2017, USGS Spectral Library Version 7: U.S. Geological Survey Data Ser.1035, doi:10.3133/ds1035
Lawrence, D. J., Elphic, R. C., Feldman, W. C., et al. 2003, JGRE, 108, 5102
Lawrence, D. J., Feldman, W. C., Barraclough, B. L., et al. 1999, GeoRL, 26, 2681
Lawrence, D. J., Feldman, W. C., Barraclough, B. L., et al. 2000, JGR, 105, 20307
Lawrence, D. J., Puetter, R. C., Elphic, R. C., et al. 2007, GeoRL, 34, L03201
Lemelin, M., Lucey, P. G., Miljković, K., et al. 2019, P&SS, 165, 230
Lemouélic, S., Langevin, Y., & Erard, S. 1999, GeoRL, 26, 1195
Lin, Y., Li, X., & Zhou, Y. 2021, LPSC, 52, 2779
Logan, L. M., Hunt, G. R., Salisbury, J. W., & Balsamo, S. R. 1973, JGR, 78, 4983
Lucey, P. G. 1998, JGR, 103, 1703
Lucey, P. G., Blewett, D. T., & Jolliff, B. L. 2000, JGR, 105, 20297
Lucey, P. G., Greenhagen, B. T., Song, E., et al. 2017, Icar, 283, 343
Lucey, P. G., Hawke, B. R., Pieters, C. M., Head, J. W., & McCord, T. B. 1986, JGR, 91, D344
Maaløe, S., & McBirney, A. R. 1997, JGRV, 76, 111
Malin, M. C. 1974, E&PSL, 21, 331
Martin, T. D. 2019, Lunar Exploration Analysis Group, 5008
McCubbin, F. M., Kaaden, K. E. V., Tartèse, R., et al. 2015, AmMin, 100, 1668
McEwen, A. S., Robinson, M. S., Eliason, E. M., et al. 1994, Sci, 266, 1858
Milliken, R. E., & Li, S. 2017, NatGe, 10, 561
Moriarty, D. P., III, & Pieters, C. M. 2016, M&PS, 51, 207
Mustard, J. F., Pieters, C. M., Isaacson, P. J., et al. 2011, JGRE, 116, E00G12
Nemchin, A. A., Pidgeon, R. T., Whitehouse, M. J., Vaughan, J. P., & Meyer, C. 2008, GeCoA, 72, 668
Peplowski, P. N., Goldsten, J. O., & Lawrence, D. L. 2014, in Int. Workshop on Instrumentation for Planetary Missions (IPM-2014) 1061, https://ssed.gsfc.nasa.gov/IPM/2014/PDF/1061.pdf
Pieters, C. M., Boardman, J., Buratti, B., et al. 2009, CSci, 96, 500
Prettyman, T. H., Hagerty, J. J., Elphic, R. C., et al. 2006, JGR, 111, E12007
Quick, J. E., James, O. B., & Albee, A. L. 1981, LPSC, 12, 117
Rogers, A. D., & Aharonson, O. 2008, JGRE, 113, E06S14
Ruff, S. W., Christensen, P. R., Blaney, D. L., et al. 2006, JGR, 111, E12S18
Ruff, S. W., & Hamilton, V. E. 2017, AmMin, 102, 235
Salisbury, J. W., & Walter, L. S. 1989, JGR, 94, 9192
Sato, H., Robinson, M. S., Hapke, B., Denevi, B. W., & Boyd, A. K. 2014, JGRE, 119, 1775

Sato, H., Robinson, M. S., Lawrence, S. J., Denevi, B. W., Hapke, B., et al. 2017, Icar, 296, 216
Schmitt, H.H., Petro, N.E., Wells, R.A., et al. 2017, Icar, 298, 2
Seddio, S. M., Jolliff, B. L., Korotev, R. L., & Carpenter, P. K. 2014, GeCoA, 135, 307
Seddio, S. M., Jolliff, B. L., Korotev, R. L., & Zeigler, R. A. 2013, AmMin, 98, 1697
Shearer, C. K., & Papike, J. J. 1993, GeCoA, 57, 4785
Shirley, K. A., & Glotch, T. D. 2019, JGRE, 124, 970
Shirley, K. A., Jaret, S. J., Thompson, L., & Glotch, T. D. 2019, LPSC, 50, 2493
Shirley, K. A., Zanetti, M., Jolliff, B. L., van der Bogert, C. H., & Hiesinger, H. 2016, Icar, 273, 214
Siegler, M. A., Feng, J., Lucey, P. G., et al. 2020, JGR, 125, e06405
Simon, J. I., Shih, C.-Y., & Nyquist, L. E. 2011, LPSC, 42, 2754
Spudis, P. D., McGovern, P. J., & Kiefer, W. S. 2013, JGRE, 118, 1063
Stadermann, A. C., Zanetti, M. R., Jolliff, B. L., et al. 2018, Icar, 309, 45
Sunshine, J. M., Besse, S., Petro, N. E., et al. 2010, LPSC, 41, 1508
Thompson, T. W. 1974, Moon, 10, 51
Vasavada, A. R., Bandfield, J. L., Greenhagen, B. T., et al. 2012, JGRE, 117, E00H18
Warren, P. H., Taylor, G. J., Keil, K., Shirley, D. N., & Wasson, J. T. 1983, E&PSL, 64, 175
Weitz, C. M., Head, J. W., & Pieters, C. M. 1998, JGR, 103, 22725
Weitz, C. M., Rutherford, M. J., Head, J. W., & McKay, D. S. 1999, M&PS, 34, 527
Whitaker, E. A. 1972, Moon, 4, 348
Wilcox, B. B., Lucey, P. G., & Hawke, B. R. 2006, JGR, 111, E09001
Wilhelms, D. E. 1987, USG Professional Paper 1348, The Geologic History of the Moon, 1348, https://doi.org/10.3133/pp1348
Williams, J.-P., Paige, D. A., Greenhagen, B. T., & Sefton-Nash, E. 2017, Icar, 283, 300
Wilson, J. T., Lawrence, D. J., Peplowski, P. N., et al. 2018, JGRE, 123, 1804
Wood, R. W. 1912, ApJ, 36, 75
Zhao, J., Xiao, L., Qiao, L., et al. 2017, JGRE, 122, 1419
Zheng, Y. C., Tsang, K. T., Chan, K. L., et al. 2012, Icar, 219, 194
Zisk, S. H., Hodges, C. A., Moore, H. J., et al. 1977, Moon, 17, 59
Zisk, S. H., Pettengill, G. H., & Catuna, G. W. 1974, Moon, 10, 17